

GVGS: Gaussian Visibility-Aware Multi-View Geometry for Accurate Surface Reconstruction

Mai Su¹, Qihan Yu¹, Zhongtao Wang¹, Yilong Li¹, Chengwei Pan², Yisong Chen¹, Guoping Wang^{1,*}

¹School of Computer Science, Peking University

²Institute of Artificial Intelligence, Beihang University

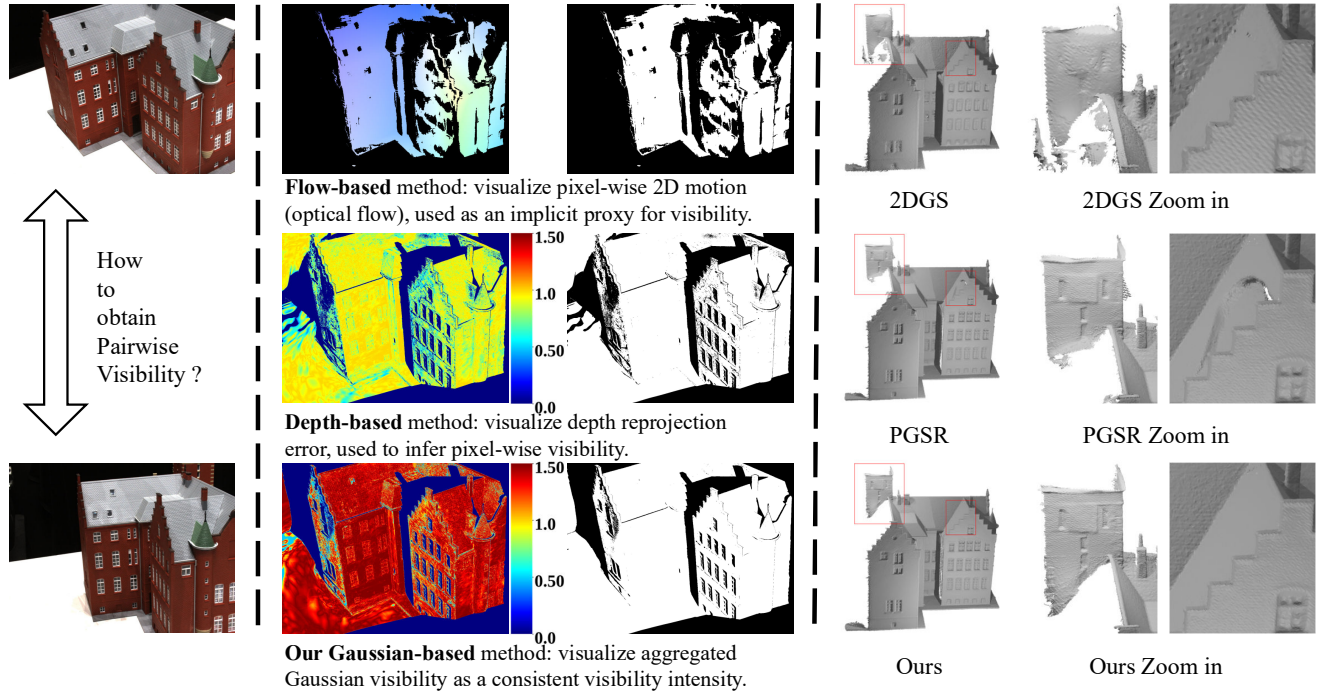


Figure 1: Reliable visibility is essential for accurate surface reconstruction. Flow-based methods infer pixel-wise correspondences from apparent 2D motion between views [24], while depth-based methods rely on cross-view depth consistency [3]; both often produce inconsistent visibility under occlusion and wide baselines. In contrast, we aggregate the visibility of shared Gaussian primitives across views, enabling more consistent pixel-wise visibility and improved surface reconstruction. For visualization, the depth-based and our Gaussian-based color maps use a shared color bar, with warmer colors indicating stronger visibility intensity.

Abstract

3D Gaussian Splatting enables efficient optimization and high-quality rendering, yet accurate surface reconstruction remains challenging. Prior methods improve surface reconstruction by refining Gaussian depth estimates, either via multi-view geometric consistency or through monocular depth priors. However, multi-view constraints become unreliable under large geometric discrepancies, while monocular priors suffer from scale ambiguity and local inconsistency, ultimately leading to inaccurate Gaussian depth supervision. To address these limitations, we introduce a Gaussian visibility-aware multi-view geometric consistency constraint that aggregates the visibility of shared Gaussian primitives across views, enabling

more accurate and stable geometric supervision. In addition, we propose a progressive quadtree-calibrated Monocular depth constraint that performs block-wise affine calibration from coarse to fine spatial scales, mitigating the scale ambiguity of depth priors while preserving fine-grained surface details. Extensive experiments on DTU and TNT datasets demonstrate consistent improvements in geometric accuracy over prior Gaussian-based and implicit surface reconstruction methods. Codes are available at an anonymous repository: <https://github.com/GVGScode/GVGS>.

1 Introduction

Recent advances in novel view synthesis show that 3D Gaussian Splatting (3DGS) [16] provides an efficient alternative to neural implicit radiance fields [1, 23, 25]. By leveraging rasterization-based rendering and directly optimizing geometric and appearance parameters, 3DGS achieves high-quality view synthesis with significantly reduced training and rendering cost. This efficiency has quickly established 3DGS as a strong foundation for large-scale and real-time scene representation. Despite its success in appearance modeling, extracting accurate and reliable surface geometry from the optimized Gaussian representation remains a fundamental challenge, since 3D Gaussian Splatting is inherently optimized for rendering rather than surface geometry extraction.

This difficulty primarily stems from the volumetric and unstructured nature of Gaussian primitives. Under purely photometric supervision, Gaussians may drift away from the true surface while still explaining image observations, leading to geometric ambiguity, thickness artifacts, and degraded multi-view consistency [32]. To alleviate these issues, recent works introduce geometry-aware regularization into the 3DGS framework, leveraging depth and normal priors or enforcing local smoothness constraints [4, 30]. However, their effectiveness remains fundamentally limited by the mismatch between volumetric Gaussian representations and the thin-surface nature of real-world geometry, especially under wide baselines, occlusions, or weakly textured regions [12, 13].

To address this gap, recent works reformulate Gaussian primitives as surface-aligned elements. Planar-based methods reinterpret anisotropic Gaussians as locally planar primitives, enabling unbiased depth and normal rendering and facilitating the integration of single-view and multi-view geometric consistency constraints [3]. In parallel, surfel-based and 2D Gaussian formulations constrain Gaussians to degenerate into disk-like surface elements, allowing explicit modeling of thin surfaces and significantly improving geometric accuracy and surface completeness [12, 13, 35]. Other hybrid approaches combine Gaussian splatting with implicit geometry fields, such as signed or unsigned distance functions, to leverage continuous distance representations for more robust surface extraction while preserving the efficiency of Gaussian-based rasterization [14, 19, 37]. Collectively, these methods highlight the importance of surface-aligned Gaussian representations for accurate surface reconstruction.

Despite these advances, existing methods still face two closely related limitations caused by unreliable Gaussian depth supervision. First, most geometric regularization strategies rely on inter-view depth consistency and become unreliable as cross-view discrepancies increase, leading to unstable multi-view supervision. Second, to compensate for this issue, monocular depth and normal priors are commonly used to refine Gaussian depth [21, 30]; however, these priors inherently suffer from scale ambiguity and local inconsistency. When applied naively, they can introduce artifacts or over-smooth fine geometric details, further degrading reconstruction quality.

To address these challenges, we propose GVGS, a geometry-

aware 3D Gaussian Splatting framework that enhances Gaussian depth supervision from both multi-view and monocular perspectives. We introduce a Gaussian visibility-aware multi-view geometric consistency constraint that aggregates the visibility of shared Gaussian primitives across views, enabling reliable geometric assessment beyond local pixel-wise depth correspondences. In addition, we propose a progressive quadtree-calibrated monocular depth constraint to locally align depth priors with Gaussian-rendered geometry, effectively mitigating scale ambiguity while preserving fine-grained surface details. Together, these components provide complementary supervision for stable optimization, yielding consistent improvements in surface accuracy over existing 3DGS-based methods.

In summary, our contributions are threefold:

- **Gaussian visibility-aware multi-view geometric consistency.** We introduce a multi-view geometric consistency that explicitly reasons about the visibility of shared Gaussian primitives across views. Aggregating Gaussian-level visibility enables more accurate and stable geometric supervision and yields high-quality pixel-wise visibility.
- **Quadtree-calibrated monocular depth constraint.** We propose a progressive quadtree-calibrated depth constraint that applies coarse-to-fine, block-wise affine alignment to monocular depth priors under geometric supervision, effectively mitigating scale ambiguity while preserving fine-grained surface details.
- **Improved mesh reconstruction from 3D Gaussian Splatting.** Building on the proposed visibility-aware geometry and calibrated depth supervision, our method achieves state-of-the-art surface accuracy and mesh quality on public benchmarks among existing 3DGS-based approaches.

2 Related Works

Novel View Synthesis Neural radiance field (NeRF) based methods model scenes as continuous volumetric fields optimized via differentiable rendering and are widely used for novel view synthesis [11, 23]. However, their reliance on dense ray marching and neural networks incurs high computational cost and long optimization times [1]. As an explicit alternative, 3D Gaussian Splatting (3DGS) represents scenes using anisotropic Gaussian primitives and performs rendering via efficient rasterization [16], enabling fast optimization and real-time or near-real-time rendering. Building on this representation, subsequent works have explored a broad range of extensions to enhance rendering quality and efficiency [7, 38], as well as to support large-scale [17, 29], dynamic [6, 22], and sparse-view scenes [5, 40].

Gaussian Splatting for Surface Reconstruction To explicitly extract surface geometry from Gaussian splatting representations, a line of work reformulates Gaussian primitives into surface-oriented representations. SuGaR is among the earliest

works to explicitly target mesh extraction from optimized 3DGS representations [12]. It introduces a surface-alignment regularizer that encourages Gaussians to form a well-distributed, locally surface-tangent configuration, and derives an approximate distance function from the Gaussian density to sample surface points and reconstruct meshes efficiently via Poisson surface reconstruction [15]. Planar-based formulations further reinterpret anisotropic Gaussians as locally planar primitives, enabling unbiased rendering of depth and normals and facilitating the integration of geometric constraints at the representation level [3]. More broadly, a number of subsequent works similarly constrain Gaussian primitives to locally planar or disk-like configurations, enabling them to better adhere to underlying surfaces for accurate geometry reconstruction [13, 35, 41]. In parallel, recent work targets transparent surface reconstruction by learning transparency attributes to handle strong view-dependent appearance and geometric ambiguities [18].

Another related direction combines Gaussian splatting with implicit geometry fields to leverage the complementary strengths of explicit and continuous representations. Methods such as GSDF and GaussianUDF jointly optimize Gaussian primitives with signed or unsigned distance functions to guide surface reconstruction while retaining efficient Gaussian-based rendering [19, 37]. Geometry Field Splatting further unifies this paradigm by representing geometry fields with Gaussian surfels and deriving an efficient differentiable rendering formulation, providing a more principled connection between Gaussian splatting and implicit geometry representations [14]. GOF represent surfaces by learning a compact, continuous opacity field over Gaussian primitives, enabling efficient and memory-compact surface reconstruction in unbounded scenes without relying on explicit distance fields or dense volumetric sampling [39].

Geometric Constraints for Gaussian-based Surface Reconstruction Beyond representation-level designs, a growing body of work improves Gaussian-based surface reconstruction by incorporating auxiliary geometric constraints during optimization. 2DGS [13] introduces a normal consistency constraint that explicitly models the surface normal of each 2D Gaussian and enforces alignment with depth-derived normals, stabilizing disk-like surface primitives during optimization. DN-Splatter [30] aligns Gaussian orientations with monocular normal priors to promote surface-aligned primitives, and further applies a local smoothness loss to enforce consistency of depth, normal, and scale among neighboring Gaussians. PGSR [3] introduces a multi-view geometric consistency loss that jointly enforces depth and photometric consistency across views by constraining shared planar Gaussian structures, drawing inspiration from classical multi-view stereo formulations [2]. These works highlight that geometric regularization is crucial for recovering accurate surfaces from Gaussian representations, yet they typically assume reliable depth estimation or consistent scale across views.

Despite their effectiveness, existing multi-view constraints rely heavily on accurate Gaussian depth estimation and are sensitive to depth bias in challenging regions. In addition, monocular supervision does not explicitly account for scale am-

biguity across views. Our method overcomes these limitations by explicitly reasoning about cross-view visibility at the Gaussian level and by introducing a quadtree-calibrated monocular depth constraint, which together enable robust multi-view geometric supervision and reliable single-view depth supervision even under biased or imperfect depth priors.

3 Method

Given a set of calibrated multi-view RGB images, we reconstruct scene geometry using Gaussian splatting by jointly leveraging multi-view geometric cues and monocular depth priors. An overview of the proposed framework is illustrated in Fig. 2. We first review the basic formulation of 3D Gaussian Splatting in Section 3.1. Section 3.2 then introduces the Gaussian visibility-aware multi-view geometric consistency. Section 3.3 presents the quadtree-calibrated depth constraint. Finally, Section 3.4 summarizes the training objective.

3.1 Preliminary: 3D Gaussian Splatting

3D Gaussian Splatting (3DGS) [16] represents a scene as a collection of learnable 3D Gaussian primitives distributed in space. Each Gaussian is parameterized by a center $\mu \in \mathbb{R}^3$ and an anisotropic covariance matrix $\Sigma \in \mathbb{R}^{3 \times 3}$, which together define its spatial extent and density contribution.

$$G(\mathbf{x}) = \exp\left(-\frac{1}{2}(\mathbf{x} - \mu)^\top \Sigma^{-1}(\mathbf{x} - \mu)\right), \quad (1)$$

where $\mathbf{x} \in \mathbb{R}^3$ denotes a 3D query location. In addition to its geometric parameters, each Gaussian is associated with an opacity value $\alpha \in [0, 1]$ and appearance features that encode view-dependent color.

During rendering, the 3D Gaussian primitives are transformed into the image plane via the camera projection, giving rise to corresponding 2D Gaussian footprints:

$$G'(\mathbf{x}') = \exp\left(-\frac{1}{2}(\mathbf{x}' - \mu')^\top \Sigma'^{-1}(\mathbf{x}' - \mu')\right), \quad (2)$$

where $\mathbf{x}' \in \mathbb{R}^2$ denotes a pixel location. The final pixel color is obtained by compositing the projected Gaussians in a depth-sorted order via alpha blending:

$$C(\mathbf{x}') = \sum_i T_i \alpha_i G'_i(\mathbf{x}') \mathbf{c}_i, \quad T_i = \prod_{j=1}^{i-1} (1 - \alpha_j G'_j(\mathbf{x}')), \quad (3)$$

where \mathbf{c}_i denotes the color of the i -th Gaussian. As the entire splatting and compositing process is fully differentiable, all Gaussian parameters can be optimized end-to-end by minimizing photometric reconstruction errors.

3.2 Gaussian Visibility-Aware Multi-View Geometric Consistency

Previous Gaussian-based surface reconstruction methods enforce multi-view geometric consistency through pixel-wise depth constraints. Specifically, these approaches reproject

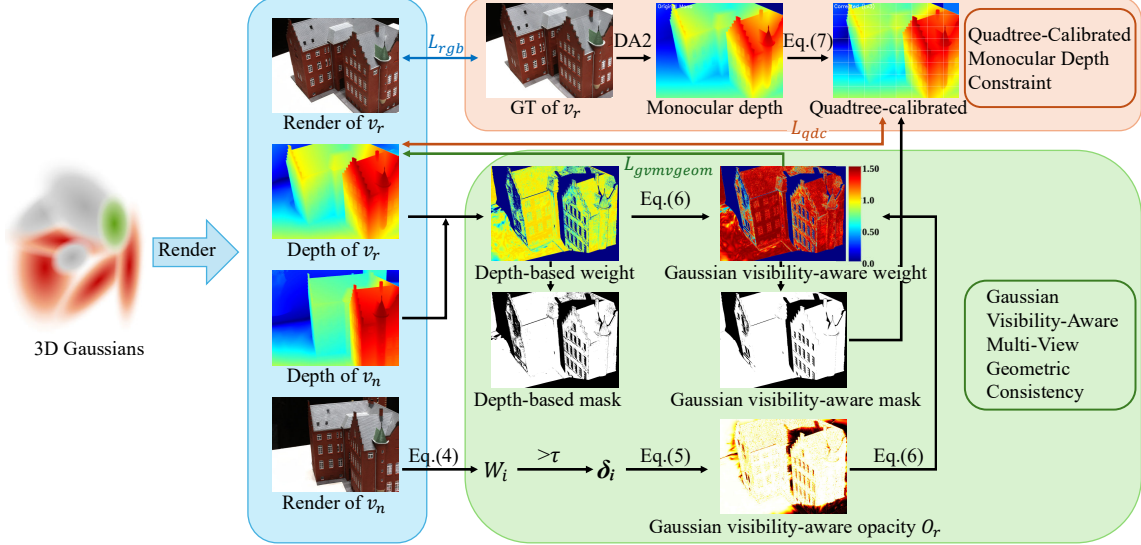


Figure 2: Overview of our GVGS. Given millions of 3D Gaussians, we render RGB images and depth maps from a reference view v_r and a neighboring view v_n . We first obtain a depth-based weight by measuring the consistency between the rendered depth maps. To explicitly reason about cross-view visibility at the Gaussian level, we render the image of v_n and compute per-Gaussian visibility weights W_i according to Eq. (4). The visibility indicator of each Gaussian in view v_n , denoted as δ_i , is then determined by thresholding $W_i > \tau$. Based on δ_i , we render a Gaussian visibility-aware opacity O_r using Eq. (5). Our final Gaussian visibility-aware weight is constructed by combining O_r with the depth-based weight, and is used to enforce the Gaussian visibility-aware multi-view geometric consistency loss $L_{gmvgeom}$. In parallel, for the ground-truth image, we predict a monocular depth map using Depth-Anything V2. This monocular depth prior is further aligned to the Gaussian-rendered depth through a quadtree-calibrated process guided by the Gaussian visibility-aware mask, and is finally used to formulate the quadtree-calibrated depth constraint L_{qdc} . Depth-based and Gaussian visibility-aware weights share the same color bar.

Gaussian-derived depth maps into neighboring views and penalize discrepancies; we refer readers to PGSR [3] for representative implementations. However, traditional multi-view geometric consistency constraints are only effective in regions where depth estimates are relatively consistent, and tend to degrade significantly in areas with large depth errors, as illustrated by the ‘‘Depth-based’’ subfigure in Fig. 1, where reprojection constraints fail on the left building facade.

To address this issue, we introduce the following principle: **multi-view geometric consistency should be enforced jointly over all pixels that are visible across neighboring views**, rather than being restricted to regions where depth reprojection is already consistent. In existing multi-view geometry methods, pixel visibility is typically inferred implicitly from depth or patch consistency, as in PMVS and its successors [8, 28]. Consequently, geometric supervision is applied only after visibility has been inferred through depth reprojection; however, accurate visibility estimation itself critically relies on reliable depth predictions, leading to a circular dependency in which visibility reasoning depends on geometry, while geometric supervision is conditioned on visibility.

We introduce a **Gaussian-based visibility estimation** to explicitly model cross-view visibility at the Gaussian level, and further develop a **Gaussian visibility-aware multi-view geometric consistency** constraint to enforce geometric consistency over co-visible regions. An overview is shown in Fig. 2.

Gaussian-based Visibility Estimation We describe a Gaussian-based approach to estimate pairwise co-visibility between views. Given a reference view v_r and a neighboring view v_n , our objective is to determine, for each pixel \mathbf{x} in v_r , whether it remains visible in v_n , yielding a co-visible mask that enables reliable geometric supervision across views.

To this end, we explicitly estimate the visibility influence of each Gaussian primitive during the differentiable rasterization of the neighboring view v_n . Following the influence formulation in EAGLES [10], we compute a per-Gaussian visibility weight $W_i \in \mathbb{R}^+$, which quantifies the accumulated alpha-compositing contribution of Gaussian primitive g_i to the rendering of view v_n :

$$W_i = \sum_{\mathbf{x} \in \Omega_n} \alpha_i(\mathbf{x}) \cdot T_i(\mathbf{x}), \quad (4)$$

where \mathbf{x} denotes a pixel location in view v_n , and Ω_n is its pixel domain. Here, $\alpha_i(\mathbf{x})$ denotes the pixel-wise opacity contribution of g_i at \mathbf{x} , and $T_i(\mathbf{x})$ is the corresponding depth-ordered transmittance under standard alpha compositing, as defined in Eq. (3). We then define a binary visibility indicator for Gaussian g_i in view v_n as $\delta_i = \mathbb{I}(W_i > \tau)$, where τ is a small threshold used to suppress negligible contributions.

We further compute a selectively accumulated opacity map in the reference view v_r as

$$O_r(\mathbf{x}) = \sum_i \delta_i \alpha_i(\mathbf{x}) \prod_{j < i} (1 - \alpha_j(\mathbf{x})), \quad (5)$$

where $\alpha_i(\mathbf{x})$ denotes the pixel-wise opacity contribution of Gaussian g_i at pixel \mathbf{x} in view v_r , computed following the standard 3D Gaussian splatting formulation. Here, δ_i serves as a visibility gate that activates the contribution of Gaussian g_i only if it is deemed visible in the neighboring view v_n . Consequently, $O_r(\mathbf{x})$ aggregates the opacity contributions of Gaussians that are co-visible in v_n when projected into the reference view v_r , while respecting the standard depth-ordered alpha compositing along each ray. Importantly, $O_r(\mathbf{x})$ is not merely an accumulation of opacity along the ray, but a Gaussian-level weighting term that explicitly encodes the pairwise visibility between the two views. Rather than accumulating opacity from all Gaussians or restricting accumulation to only visible ones, our formulation retains the complete alpha-compositing structure and selectively gates the effective contributions using the cross-view visibility indicator δ_i . This design enables consistent geometric supervision even in regions where depth-based reprojection fails, as illustrated in the “Our Gaussian-based” subfigure of Fig. 1, where co-visible Gaussians on the facade are correctly aggregated despite large cross-view depth discrepancies.

Gaussian Visibility-Aware Multi-View Geometric Consistency We build upon the multi-view geometric consistency loss L_{mvgeom} introduced in PGSR [3]. Specifically, each reference pixel \mathbf{x} is associated with a forward–backward reprojection error $\phi(\mathbf{x})$, which is mapped to a pixel-wise confidence weight via a monotonic activation function, e.g., $\exp(-\phi(\mathbf{x}))$. This weighting scheme assigns lower confidence to pixels with large reprojection errors. In practice, pixels whose reprojection error exceeds a predefined threshold (e.g., $\phi(\mathbf{x}) > 1$) are excluded from the multi-view geometric consistency loss. We extend this formulation by explicitly incorporating shared Gaussian-level visibility information, denoted as $O_r(\mathbf{x})$, which enables geometric supervision to be applied over a broader set of co-visible regions. This effect is evidenced by the comparison between the “Depth-based weight” and the “Gaussian visibility-aware weight” in Fig. 2, where previously unsupervised facade regions become effectively constrained.

The resulting Gaussian visibility-aware multi-view geometric consistency loss is defined as

$$L_{gmvgeom} = \frac{1}{|\mathcal{V}|} \sum_{\mathbf{x} \in \mathcal{V}} (\exp(-\phi(\mathbf{x})) + \lambda O_r(\mathbf{x})) \phi(\mathbf{x}), \quad (6)$$

where \mathcal{V} is constructed as the union of two subsets: (i) pixels that pass the conventional depth-based reprojection consistency check, and (ii) pixels that are identified as co-visible by our Gaussian visibility-aware opacity. As illustrated in Fig. 2, the resulting region \mathcal{V} corresponds to the “Gaussian visibility-aware mask”. The parameter λ controls the relative contribution of the visibility term.

3.3 Quadtree-calibrated Monocular Depth Constraint

Recent advances in large-scale vision models have enabled highly detailed monocular depth prediction from a single im-

age [33, 34]. When used in multi-view reconstruction pipelines, however, such monocular depth maps exhibit two inherent limitations: *scale ambiguity* and *view-dependent bias*. To alleviate these issues, existing Gaussian-based reconstruction methods typically apply a global scale-and-shift calibration using sparse COLMAP SfM points, or apply depth supervision only to pixels that satisfy multi-view reprojection consistency [9, 17]. Nevertheless, these strategies remain insufficient to resolve spatially varying depth bias, and monocular depth predictions often stay misaligned with Gaussian-rendered depth, leading to biased geometric gradients and unstable optimization.

We propose a quadtree-calibrated monocular depth alignment scheme that progressively performs local depth calibration using Gaussian-rendered depth as an in-training geometric reference.

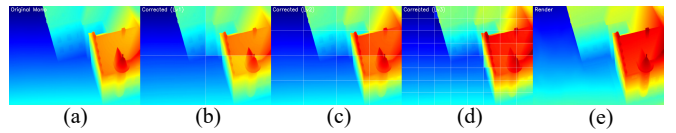


Figure 3: Progressive quadtree-calibrated depth calibration. (a) Raw monocular depth prediction from Depth-Anything v2 [34] and (e) the Gaussian-rendered depth, exhibiting clear depth bias and misalignment, especially in the roof regions on the right. (b–d) Depth maps after progressive quadtree-based calibration at increasing levels (Lv1–Lv3), where block-wise affine calibration is applied from coarse to fine. As the quadtree level increases, the calibrated monocular depth becomes progressively better aligned with the Gaussian-rendered depth.

Coarse-to-fine quadtree depth calibration. During training, we employ a coarse-to-fine quadtree schedule by selecting a split level $L(t) \in \{0, \dots, L_{\max}\}$ at iteration t and partitioning the image into $2^{L(t)} \times 2^{L(t)}$ uniformly sized blocks. As training proceeds, $L(t)$ is gradually increased, enabling the depth calibration to transition from a global, coarse alignment to finer-grained, locally adaptive refinements.

For each quadtree block \mathcal{B}_k induced at iteration t , we calibrate the monocular depth $D_m(\mathbf{x})$ to the Gaussian-rendered depth $D_g(\mathbf{x})$ using a block-wise affine model [27],

$$\begin{aligned} D'_m(\mathbf{x}) &= a_k D_m(\mathbf{x}) + b_k, \quad \mathbf{x} \in \mathcal{B}_k \cap \mathcal{V}, \\ a_k &= \frac{\sigma_{\mathbf{y} \in \mathcal{B}_k}(D_g(\mathbf{y}))}{\sigma_{\mathbf{y} \in \mathcal{B}_k}(D_m(\mathbf{y}))}, \\ b_k &= \mu_{\mathbf{y} \in \mathcal{B}_k}(D_g(\mathbf{y}) - a_k D_m(\mathbf{y})), \end{aligned} \quad (7)$$

where (a_k, b_k) denote the affine calibration parameters associated with block \mathcal{B}_k . Here, $\mu(\cdot)$ and $\sigma(\cdot)$ denote robust estimators of location and scale, respectively, implemented as the median and the mean absolute deviation about the median. These parameters are robustly estimated over pixels within each block \mathcal{B}_k , which reduces the influence of outliers and unreliable depth predictions. Furthermore, depth calibration is restricted to the pixel set \mathcal{V} defined in Eq. (6), comprising pixels that

are either validated by inter-view reprojection consistency or identified as co-visible through Gaussian visibility. Importantly, the block-wise affine parameters are recomputed only when the quadtree level $L(t)$ increases and are reused across subsequent iterations, introducing negligible computational overhead during training. As illustrated in Fig. 3, this progressive schedule enables depth calibration to be refined from coarse to fine spatial scales, yielding increasingly better alignment with the Gaussian-rendered depth, particularly in regions that exhibit large initial depth bias, such as the rooftop.

Quadtree-calibrated Monocular Depth Constraint The calibrated monocular depth is then supervised against the Gaussian-rendered depth using an ℓ_1 loss,

$$L_{qdc} = \sum_{\mathbf{x} \in \mathcal{V}} \|D'_m(\mathbf{x}) - D_g(\mathbf{x})\|_1, \quad (8)$$

where \mathcal{V} denotes the set of pixels selected for geometric supervision, as defined in Eq. (6). Depth alignment is estimated and applied exclusively within this trusted region, thereby avoiding contamination from background areas and unreliable depth predictions. Through coarse-to-fine quadtree-based alignment, we provide the Gaussians with stable and accurate monocular depth supervision that preserves local geometric details while remaining robust to noisy depth estimates.

3.4 Training Objective

The overall training objective is formulated as a weighted sum of multiple loss terms:

$$L = L_{rgb} + \lambda_1 L_s + \lambda_2 L_{mvrgb} + \lambda_3 L_{gmvgeom} + \lambda_4 L_{qdc}, \quad (9)$$

where λ_1 – λ_4 are scalar weights that balance the contributions of the individual loss terms.

Here, L_{rgb} denotes the standard photometric reconstruction loss in 3D Gaussian Splatting, which combines ℓ_1 and SSIM terms. Following PGSR, we directly adopt single-view depth and normal supervision via L_s , together with a multi-view photometric consistency loss L_{mvrgb} [3]. Building upon these components, we introduce our proposed Gaussian visibility-aware multi-view geometric consistency loss $L_{gmvgeom}$ and the quadtree-calibrated monocular depth loss L_{qdc} , which together enable robust geometric supervision and adaptive calibration of monocular depth priors throughout training.

4 Experiments

4.1 Datasets

We evaluate our method on two standard benchmarks for multi-view surface reconstruction: **DTU** and **Tanks and Temples (TNT)**. The DTU dataset consists of calibrated indoor scenes with high-quality structured-light ground-truth geometry. Following prior work [3], we report results on the standard set of 15 scans using the symmetric Chamfer Distance, without performing any explicit alignment between the reconstructed

geometry and the ground-truth point cloud. We use the DTU data preprocessed by 2DGS [13].

The Tanks and Temples (TNT) benchmark includes large-scale indoor and outdoor scenes. We evaluate on the standard *Intermediate* set comprising six scenes (Barn, Caterpillar, Courthouse, Ignatius, Meetingroom, and Truck), and report per-scene F-score (F1). We adopt the TNT data provided by GOF [39] and follow the evaluation protocol of QGS [41].

4.2 Implementation Details

Our implementation builds upon PGSR [3], inheriting most default hyperparameters, and uses monocular depth priors from Depth Anything v2 [34], which are further calibrated via the proposed quadtree-calibrated depth constraint. For DTU, each scene is trained for 30k iterations, during which the quadtree split level $L(t)$ is progressively increased at 10k, 15k, and 20k iterations. The quadtree-calibrated monocular depth loss L_{qdc} is activated from 7k to 25k iterations to ensure stable optimization. Negligible Gaussian contributions are filtered using a threshold $\tau = 0.01$, with Gaussians below this threshold considered non-visible in the neighboring view. We set the visibility weighting coefficient λ in Eq. (6) to 0.5. For Tanks and Temples (TNT), each scene is trained for 60k iterations with corresponding hyperparameters adjusted accordingly. Meshes are extracted via TSDF fusion [26]. All experiments are conducted on an Ubuntu server equipped with four NVIDIA A6000 GPUs (48 GB memory each). Additional implementation details are provided in our code.

4.3 Comparison

For geometry evaluation, we follow the standard protocol of recent Gaussian-based methods and conduct all experiments on DTU and TNT at *half resolution*. Chamfer Distance and F-score are reported as the primary geometry metrics. We quantitatively compare our method with implicit surface methods [20, 31, 36] and Gaussian-based surface reconstruction approaches [3, 12, 13, 16, 39, 41], using numerical results directly taken from the recent QGS paper under a unified evaluation setup [41].

For DTU dataset, as shown in Table 1, our method achieves the best Chamfer Distance on **14 out of the 15** evaluated scans. In terms of overall accuracy, our approach attains a mean Chamfer Distance of **0.50 mm (0.4966 mm before rounding)**, improving upon the best prior result by approximately **7%**. As illustrated in Fig. 5, our method produces more complete rabbit ears, smoother skull forehead surfaces, more faithful reconstruction of dental cavities, and a clearer separation between the bird’s feet and the supporting base. We attribute these improvements to the stronger geometric constraints introduced by our method, which provide more reliable supervision in regions with uneven illumination and sparse viewpoints. Despite additional geometric supervision, our method incurs only minimal overhead and maintains comparable training efficiency to existing Gaussian-based approaches.

For the Tanks and Temples benchmark, Table 2 reports the quantitative F1-score results. Our method achieves the high-

Table 1: **Chamfer Distance on DTU (lower is better).** For each scan, the best, second, and third results are highlighted with red, orange, and yellow backgrounds, respectively.

CD (mm)↓	24	37	40	55	63	65	69	83	97	105	106	110	114	118	122	Mean	Time
NeuS [31]	1.00	1.37	0.93	0.43	1.10	0.65	0.57	1.48	1.09	0.83	0.52	1.20	0.35	0.49	0.54	0.84	>12h
VolSDF [36]	1.14	1.26	0.81	0.49	1.25	0.70	0.72	1.29	1.18	0.70	0.66	1.08	0.42	0.61	0.55	0.86	>12h
Neuralangelo [20]	0.37	0.72	0.35	0.35	0.87	0.54	0.53	1.29	0.97	0.73	0.47	0.74	0.32	0.41	0.43	0.61	>128h
3DGs [16]	2.14	1.53	2.08	1.68	3.49	2.21	1.43	2.07	2.22	1.75	1.79	2.55	1.53	1.52	1.50	1.96	11.2min
SuGaR [12]	1.47	1.33	1.13	0.61	2.25	1.71	1.15	1.63	1.62	1.07	0.79	2.45	0.98	0.88	0.79	1.33	1h
2DGs [13]	0.48	0.91	0.39	0.39	1.01	0.83	0.81	1.36	1.27	0.76	0.70	1.40	0.40	0.76	0.52	0.80	19.2min
GOF [39]	0.50	0.82	0.37	0.37	1.12	0.74	0.73	1.18	1.29	0.68	0.77	0.90	0.42	0.66	0.49	0.74	1h
PGSR [3]	0.40	0.60	0.39	0.37	0.78	0.59	0.53	1.18	0.67	0.63	0.48	0.62	0.34	0.42	0.39	0.56	40min
QGS [41]	0.38	0.62	0.37	0.38	0.75	0.55	0.51	1.12	0.68	0.61	0.46	0.58	0.35	0.41	0.40	0.54	48min
Ours	0.33	0.54	0.34	0.32	0.79	0.52	0.47	1.04	0.62	0.58	0.38	0.55	0.30	0.34	0.33	0.50	43min

F1-Score↑	N-angelo	2DGs	GOF	PGSR	QGS	Ours
Barn	0.70	0.41	0.51	0.52	0.55	0.58
Caterpillar	0.36	0.24	0.41	0.38	0.40	0.47
Courthouse	0.28	0.16	0.28	0.26	0.28	0.24
Ignatius	0.89	0.52	0.68	0.77	0.81	0.81
Meetingroom	0.32	0.17	0.28	0.29	0.31	0.39
Truck	0.48	0.45	0.58	0.62	0.64	0.68
Mean	0.50	0.33	0.46	0.47	0.50	0.53
Time	>127h	34min	114min	66min	75min	117min

Table 2: **Quantitative F1-score comparison on the TNT dataset** (higher is better). The best/second/third results are highlighted in red, orange, and yellow.

est average F1-score of **0.53** (**0.5302** before rounding) across all evaluated scenes, outperforming all compared approaches. Specifically, it attains the best performance on three out of the six scenes and ranks second on two scenes, indicating strong and consistent reconstruction quality. As illustrated in Fig. 5, only our method successfully reconstructs the *Caterpillar* bucket without holes and avoids depth artifacts on the left side. Moreover, our approach is the only one that correctly recovers the pillar beneath the staircase and the associated wall details in the *Courthouse* scene, and it also achieves the most faithful reconstruction of the hollow wheel hub structures in the *Truck* scene. More qualitative results demonstrating our accurate surface reconstruction are shown in Fig. 6(a).

We also present additional comparisons of visibility masks generated by the flow-based method DPFFlow [24] and the depth-based PGSR [3] in Fig. 6(b). We observe that flow-based visibility tends to be noisy and unstable, while depth-based visibility is sensitive to depth inaccuracies. In contrast, our method produces cleaner and more coherent visibility masks.

4.4 Ablation Studies

We perform ablation studies to evaluate the contribution of each component in our framework. Beginning with the full model (**Full**), components are progressively removed. First, the quadtree-calibrated depth constraint is disabled, and Gaussian depth is directly supervised using monocular depth predicted by

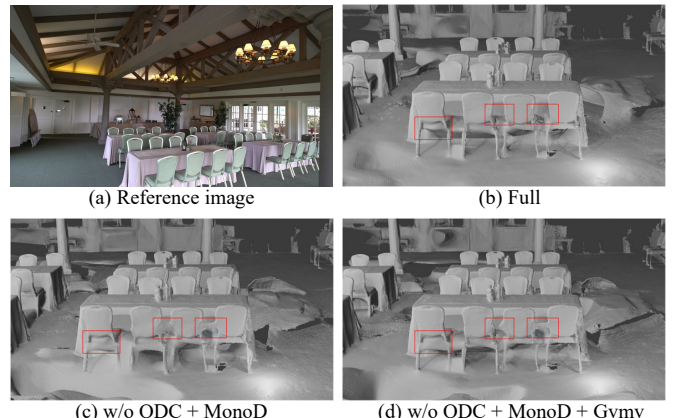


Figure 4: Qualitative ablation of the proposed components on *Meetingroom*. Red boxes highlight failure cases.

Setting	d2s CD ↓	s2d CD ↓	Mean CD ↓
Full	0.497	0.496	0.497
w/o QDC	0.507	0.504	0.505
w/o QDC + MonoD	0.503	0.520	0.512
w/o QDC + MonoD + Gvmv	0.503	0.530	0.516

Table 3: Ablation study on the DTU dataset. Lower Chamfer Distance (CD) indicates better performance.

Depth Anything V2 [34] (**w/o QDC**). Next, monocular depth supervision is removed (**w/o QDC + MonoD**), followed by the removal of the Gaussian visibility-aware multi-view geometric consistency term (**w/o QDC + MonoD + GVMV**).

As shown in Table 3, ablation results on the DTU dataset indicate that removing any individual component consistently degrades reconstruction accuracy. We further visualize the ablation results on the *Meetingroom* scene from the Tanks and Temples benchmark in Fig. 4, where the progressive degradation in surface quality of the chairs confirms that each component plays a complementary role.

5 Conclusion

In this work, we focus on Gaussian-based surface reconstruction and introduce a Gaussian visibility-aware multi-view geometric consistency formulation together with a quadtree-calibrated monocular depth constraint, which jointly provide richer and more comprehensive geometric guidance during optimization and lead to consistent improvements in surface reconstruction quality.

In addition, our method produces high-quality multi-view visibility masks as a natural byproduct. Beyond their use in surface reconstruction, these visibility estimates are broadly applicable to a wide range of tasks, including multi-view semantic segmentation, scene understanding, and geometry-aware rendering and editing. We hope that this additional capability will inspire future work to further explore Gaussian-based visibility reasoning as a general geometric prior for multi-view vision and graphics.

References

- [1] Jonathan T Barron, Ben Mildenhall, Matthew Tancik, Peter Hedman, Ricardo Martin-Brualla, and Pratul P Srinivasan. Mip-nerf: A multiscale representation for anti-aliasing neural radiance fields. In *Proceedings of the IEEE/CVF international conference on computer vision*, pages 5855–5864, 2021.
- [2] Neill DF Campbell, George Vogiatzis, Carlos Hernández, and Roberto Cipolla. Using multiple hypotheses to improve depth-maps for multi-view stereo. In *European conference on computer vision*, pages 766–779. Springer, 2008.
- [3] Danpeng Chen, Hai Li, Weicai Ye, Yifan Wang, Weijian Xie, Shangjin Zhai, Nan Wang, Haomin Liu, Hujun Bao, and Guofeng Zhang. Pgss: Planar-based gaussian splatting for efficient and high-fidelity surface reconstruction. *IEEE Transactions on Visualization and Computer Graphics*, 2024.
- [4] Hanlin Chen, Fangyin Wei, Chen Li, Tianxin Huang, Yunsong Wang, and Gim Hee Lee. Vcr-gaus: View consistent depth-normal regularizer for gaussian surface reconstruction. *Advances in Neural Information Processing Systems*, 37:139725–139750, 2024.
- [5] Yuedong Chen, Haofei Xu, Chuanxia Zheng, Bohan Zhuang, Marc Pollefeys, Andreas Geiger, Tat-Jen Cham, and Jianfei Cai. Mvsplat: Efficient 3d gaussian splatting from sparse multi-view images. In *European Conference on Computer Vision*, pages 370–386. Springer, 2024.
- [6] Yuanxing Duan, Fangyin Wei, Qiyu Dai, Yuhang He, Wenzheng Chen, and Baoquan Chen. 4d-rotor gaussian splatting: towards efficient novel view synthesis for dynamic scenes. In *ACM SIGGRAPH 2024 Conference Papers*, pages 1–11, 2024.
- [7] Guangchi Fang and Bing Wang. Mini-splatting: Representing scenes with a constrained number of gaussians. In *European Conference on Computer Vision*, pages 165–181. Springer, 2024.
- [8] Yasutaka Furukawa and Jean Ponce. Accurate, dense, and robust multiview stereopsis. *IEEE Transactions on Pattern Analysis and Machine Intelligence*, 32(8):1362–1376, 2010.
- [9] Yuanyuan Gao, Hao Li, Jiaqi Chen, Zhengyu Zou, Zhihang Zhong, Dingwen Zhang, Xiao Sun, and Junwei Han. Citygs-x: A scalable architecture for efficient and geometrically accurate large-scale scene reconstruction. *arXiv preprint arXiv:2503.23044*, 2025.
- [10] Sharath Girish, Kamal Gupta, and Abhinav Shrivastava. Eagles: Efficient accelerated 3d gaussians with lightweight encodings. In *European Conference on Computer Vision*, pages 54–71. Springer, 2024.
- [11] Xiaodong Gu, Zhiwen Fan, Siyu Zhu, Zuozhuo Dai, Feitong Tan, and Ping Tan. Cascade cost volume for high-resolution multi-view stereo and stereo matching. In *Proceedings of the IEEE/CVF conference on computer vision and pattern recognition*, pages 2495–2504, 2020.
- [12] Antoine Guédon and Vincent Lepetit. Sugar: Surface-aligned gaussian splatting for efficient 3d mesh reconstruction and high-quality mesh rendering. In *Proceedings of the IEEE/CVF Conference on Computer Vision and Pattern Recognition*, pages 5354–5363, 2024.
- [13] Binbin Huang, Zehao Yu, Anpei Chen, Andreas Geiger, and Shenghua Gao. 2d gaussian splatting for geometrically accurate radiance fields. In *ACM SIGGRAPH 2024 conference papers*, pages 1–11, 2024.
- [14] Kaiwen Jiang, Venkataram Sivaram, Cheng Peng, and Ravi Ramamoorthi. Geometry field splatting with gaussian surfels. In *Proceedings of the Computer Vision and Pattern Recognition Conference*, pages 5752–5762, 2025.
- [15] Michael Kazhdan, Matthew Bolitho, and Hugues Hoppe. Poisson surface reconstruction. In *Proceedings of the fourth Eurographics symposium on Geometry processing*, volume 7, 2006.
- [16] Bernhard Kerbl, Georgios Kopanas, Thomas Leimkühler, and George Drettakis. 3d gaussian splatting for real-time radiance field rendering. *ACM Trans. Graph.*, 42(4):139–1, 2023.
- [17] Bernhard Kerbl, Andreas Meuleman, Georgios Kopanas, Michael Wimmer, Alexandre Lanvin, and George Drettakis. A hierarchical 3d gaussian representation for real-time rendering of very large datasets. *ACM Transactions on Graphics (TOG)*, 43(4):1–15, 2024.

[18] Mingwei Li, Pu Pang, Hehe Fan, Hua Huang, and Yi Yang. Tsgs: Improving gaussian splatting for transparent surface reconstruction via normal and de-lighting priors. In *Proceedings of the 33rd ACM International Conference on Multimedia*, pages 7220–7229, 2025.

[19] Shujuan Li, Yu-Shen Liu, and Zhizhong Han. Gaussianudf: Inferring unsigned distance functions through 3d gaussian splatting. In *Proceedings of the Computer Vision and Pattern Recognition Conference*, pages 27113–27123, 2025.

[20] Zhaoshuo Li, Thomas Müller, Alex Evans, Russell H Taylor, Mathias Unberath, Ming-Yu Liu, and Chen-Hsuan Lin. Neuralangelo: High-fidelity neural surface reconstruction. In *Proceedings of the IEEE/CVF Conference on Computer Vision and Pattern Recognition*, pages 8456–8465, 2023.

[21] Zhihao Liang, Qi Zhang, Ying Feng, Ying Shan, and Kui Jia. Gs-ir: 3d gaussian splatting for inverse rendering. In *Proceedings of the IEEE/CVF Conference on Computer Vision and Pattern Recognition*, pages 21644–21653, 2024.

[22] Jonathon Luiten, Georgios Kopanas, Bastian Leibe, and Deva Ramanan. Dynamic 3d gaussians: Tracking by persistent dynamic view synthesis. In *2024 International Conference on 3D Vision (3DV)*, pages 800–809. IEEE, 2024.

[23] Ben Mildenhall, Pratul P Srinivasan, Matthew Tancik, Jonathan T Barron, Ravi Ramamoorthi, and Ren Ng. Nerf: Representing scenes as neural radiance fields for view synthesis. *Communications of the ACM*, 65(1):99–106, 2021.

[24] Henrique Morimitsu, Xiaobin Zhu, Roberto M Cesar, Xiangyang Ji, and Xu-Cheng Yin. Dpflow: Adaptive optical flow estimation with a dual-pyramid framework. In *Proceedings of the Computer Vision and Pattern Recognition Conference*, pages 17810–17820, 2025.

[25] Thomas Müller, Alex Evans, Christoph Schied, and Alexander Keller. Instant neural graphics primitives with a multiresolution hash encoding. *ACM transactions on graphics (TOG)*, 41(4):1–15, 2022.

[26] Richard A Newcombe, Shahram Izadi, Otmar Hilliges, David Molyneaux, David Kim, Andrew J Davison, Pushmeet Kohi, Jamie Shotton, Steve Hodges, and Andrew Fitzgibbon. Kinectfusion: Real-time dense surface mapping and tracking. In *2011 10th IEEE international symposium on mixed and augmented reality*, pages 127–136. Ieee, 2011.

[27] René Ranftl, Katrin Lasinger, David Hafner, Konrad Schindler, and Vladlen Koltun. Towards robust monocular depth estimation: Mixing datasets for zero-shot cross-dataset transfer. *IEEE transactions on pattern analysis and machine intelligence*, 44(3):1623–1637, 2020.

[28] S.M. Seitz, B. Curless, J. Diebel, D. Scharstein, and R. Szeliski. A comparison and evaluation of multi-view stereo reconstruction algorithms. In *2006 IEEE Computer Society Conference on Computer Vision and Pattern Recognition (CVPR’06)*, volume 1, pages 519–528, 2006.

[29] Mai Su, Zhongtao Wang, Huishan Au, Yilong Li, Xizhe Cao, Chengwei Pan, Yisong Chen, and Guoping Wang. Hug: Hierarchical urban gaussian splatting with block-based reconstruction for large-scale aerial scenes. In *Proceedings of the IEEE/CVF International Conference on Computer Vision*, pages 28839–28848, 2025.

[30] Matias Turkulainen, Xuqian Ren, Iaroslav Melekhov, Otto Seiskari, Esa Rahtu, and Juho Kannala. Dn-splatter: Depth and normal priors for gaussian splatting and meshing. In *2025 IEEE/CVF Winter Conference on Applications of Computer Vision (WACV)*, pages 2421–2431. IEEE, 2025.

[31] Peng Wang, Lingjie Liu, Yuan Liu, Christian Theobalt, Taku Komura, and Wenping Wang. Neus: Learning neural implicit surfaces by volume rendering for multi-view reconstruction. *arXiv preprint arXiv:2106.10689*, 2021.

[32] Yuru Xiao, Deming Zhai, Wenbo Zhao, Kui Jiang, Junjun Jiang, and Xianming Liu. Mcgs: Multiview consistency enhancement for sparse-view 3d gaussian radiance fields. *IEEE Transactions on Pattern Analysis and Machine Intelligence*, 2025.

[33] Gangwei Xu, Haotong Lin, Hongcheng Luo, Xianqi Wang, Jingfeng Yao, Lianghui Zhu, Yuechuan Pu, Cheng Chi, Haiyang Sun, Bing Wang, et al. Pixel-perfect depth with semantics-prompted diffusion transformers. *arXiv preprint arXiv:2510.07316*, 2025.

[34] Lihe Yang, Bingyi Kang, Zilong Huang, Zhen Zhao, Xiaogang Xu, Jiashi Feng, and Hengshuang Zhao. Depth anything v2. *Advances in Neural Information Processing Systems*, 37:21875–21911, 2024.

[35] Yixin Yang, Yang Zhou, and Hui Huang. Introducing unbiased depth into 2d gaussian splatting for high-accuracy surface reconstruction. In *Computer Graphics Forum*, volume 44, page e70252. Wiley Online Library, 2025.

[36] Lior Yariv, Jiatao Gu, Yoni Kasten, and Yaron Lipman. Volume rendering of neural implicit surfaces. *Advances in neural information processing systems*, 34:4805–4815, 2021.

[37] Mulin Yu, Tao Lu, Linning Xu, Lihan Jiang, Yuanbo Xiangli, and Bo Dai. Gsdf: 3dgs meets sdf for improved neural rendering and reconstruction. *Advances in Neural Information Processing Systems*, 37:129507–129530, 2024.

- [38] Zehao Yu, Anpei Chen, Binbin Huang, Torsten Sattler, and Andreas Geiger. Mip-splatting: Alias-free 3d gaussian splatting. In *Proceedings of the IEEE/CVF conference on computer vision and pattern recognition*, pages 19447–19456, 2024.
- [39] Zehao Yu, Torsten Sattler, and Andreas Geiger. Gaussian opacity fields: Efficient adaptive surface reconstruction in unbounded scenes. *ACM Transactions on Graphics (ToG)*, 43(6):1–13, 2024.
- [40] Chuanrui Zhang, Yingshuang Zou, Zhuoling Li, Minmin Yi, and Haoqian Wang. Transplat: Generalizable 3d gaussian splatting from sparse multi-view images with transformers. In *Proceedings of the AAAI Conference on Artificial Intelligence*, volume 39, pages 9869–9877, 2025.
- [41] Ziyu Zhang, Binbin Huang, Hanqing Jiang, Liyang Zhou, Xiaojun Xiang, and Shuhan Shen. Quadratic gaussian splatting: High quality surface reconstruction with second-order geometric primitives. In *Proceedings of the IEEE/CVF International Conference on Computer Vision*, pages 28260–28270, 2025.

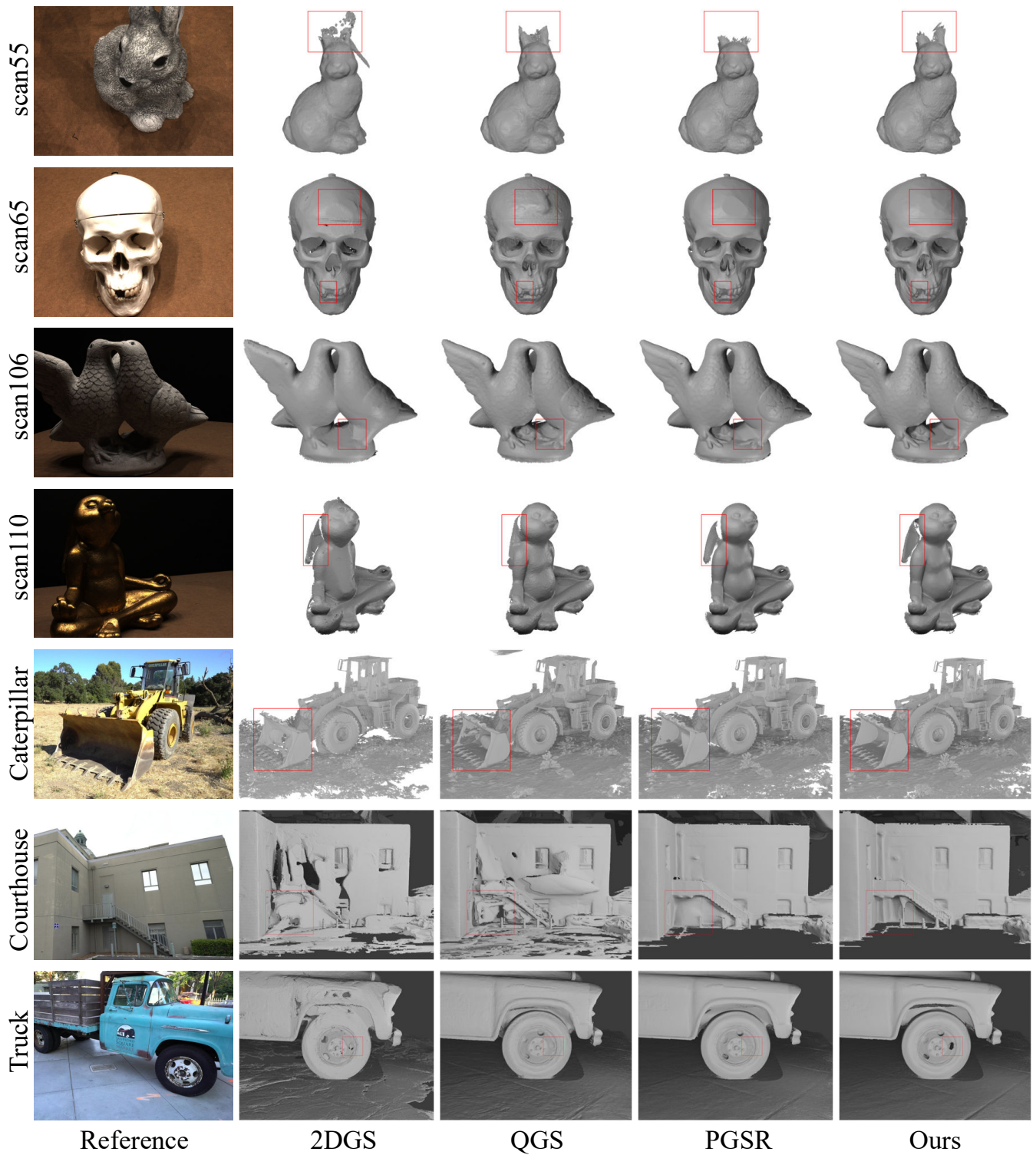
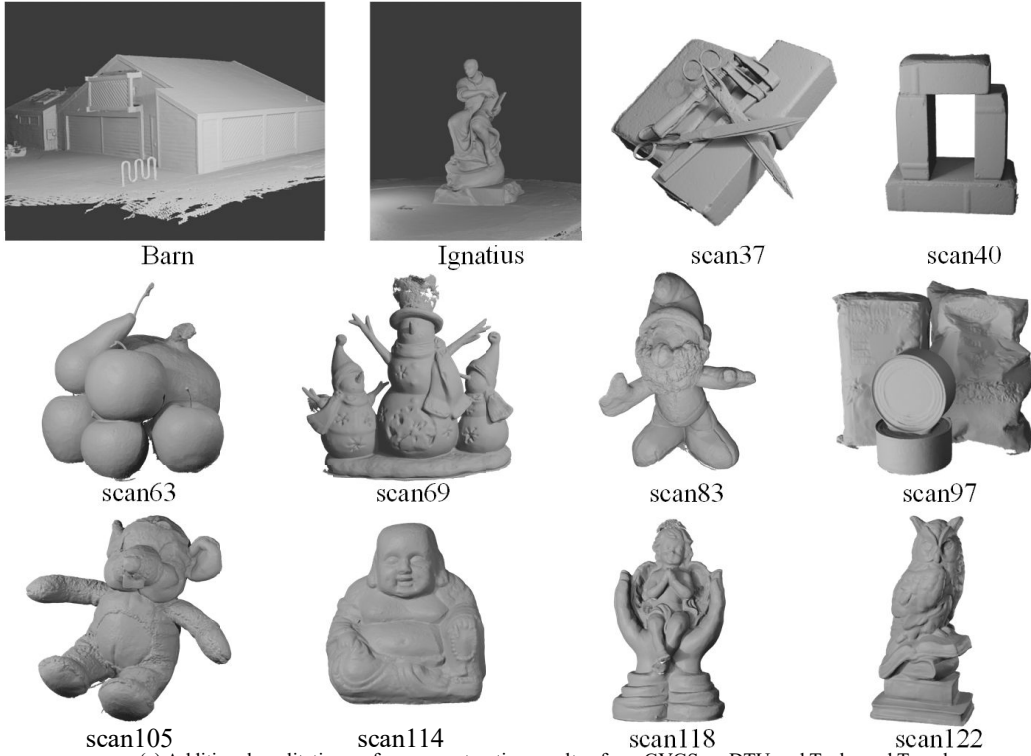
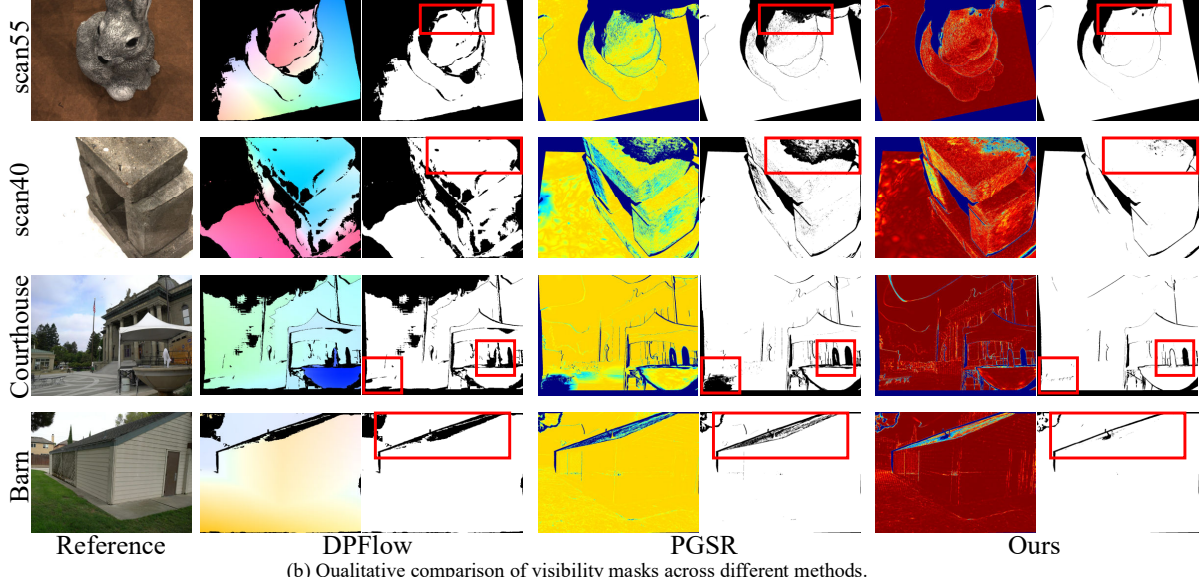


Figure 5: Qualitative Comparison of Reconstructed Geometry with Related Works on DTU and Tanks and Temples. Red boxes highlight regions with noticeable geometric differences.



(a) Additional qualitative surface reconstruction results of our GVGS on DTU and Tanks and Temples.



(b) Qualitative comparison of visibility masks across different methods.

Figure 6: Qualitative results of surface reconstruction and visibility estimation. (a) Surface reconstruction results of our GVGS on the DTU and Tanks and Temples datasets. (b) Qualitative comparison of visibility masks across different methods. The color visualization of DPFlow reflects 2D motion magnitude derived from optical flow, PGSR visualizes pixel-wise visibility weights inferred from photometric reprojection errors, while our method visualizes visibility weights obtained by aggregating the visibility of shared Gaussian primitives across views, producing cleaner and more coherent visibility.